

Article

In Silico Interactome of a Room-Temperature Ferroelectric Nematic Material

Richard J. Mandle ^{1,2} ¹ School of Physics and Astronomy, University of Leeds, Leeds LS2 9JT, UK; r.mandle@leeds.ac.uk² School of Chemistry, University of Leeds, Leeds LS2 9HT, UK

Abstract: The ferroelectric nematic (N_F) phase, characterised by the combination of orientational and polar order, offers unique properties that are challenging to replicate in other systems. Understanding the molecular structure requirements for generating the N_F phase is crucial for the design of new materials with enhanced properties. This study investigates UUQU-4-N, a room-temperature N_F material, using fully atomistic molecular dynamics simulations. UUQU-4-N does not spontaneously form an apolar nematic phase in silico, but exhibits a stable polar nematic configuration akin to the N_F phase. The polar order remains significant and near saturation throughout the simulations. The study also examines the cylindrical pair correlation functions, providing insights into the preferred pairing modes and intermolecular interactions which we can then attribute to specific molecular features. We then simulate structural variants of UUQU-4-N, highlighting the potential for developing further examples of near-room-temperature ferroelectric nematic materials via the manipulation of the fluorination pattern, variations in terminal chain length, and replacement of the difluoromethyleneoxy linker.

Keywords: liquid crystals; ferroelectrics; nematics; ferroelectric nematic

1. Introduction

The nematic phase (N) is the simplest liquid crystal phase, and features molecules which have some sort of shape anisotropy (rods, disks, etc.) and are positionally disordered with some degree of orientational order along a common direction known as the director. The ferroelectric nematic (N_F) phase is the most recently discovered nematic phase variant, in which the orientational order of the ‘classical’ nematic phase is augmented with a polar order [1–5]. This polar order endows the N_F phase—and the materials that exhibit it—with remarkable properties, the combination of which is difficult if not impossible to replicate in other systems [6–9]. The design of new molecules and materials that exhibit the N_F phase is in its earliest stages; from Refs. [10–23], we know little about how molecular structure generates this phase, with the majority of materials known to exhibit it being derivatives of either RM734 [11] or DIO [24]. It stands to reason that, if we understood which parts of a molecule’s structure are key for generating the N_F phase, we would be able to synthesise ‘better’ materials with (relative) ease.

The material known as UUQU-4-N (Figure 1) [25] is an interesting example of an N_F material which does not derive from RM734/DIO. UUQU-4-N is heavily fluorinated, with the fluorination pattern (and also the difluoromethoxy and nitrile units) contributing to a large molecular electric dipole moment of circa 11 Debye (*supra vide*). Experimentally, UUQU-4-N exhibits a direct isotropic-to- N_F transition which occurs around room temperature; if—in some hypothetical descendent material of UUQU-4-N—the clearing point could be increased slightly (~30 °C) and the melting point brought down by a similar magnitude, then one might expect a *bona fide* single-component near-room-temperature N_F material—in effect, something akin to the 5CB of N_F research.



Citation: Mandle, R.J. In Silico Interactome of a Room-Temperature Ferroelectric Nematic Material. *Crystals* **2023**, *13*, 857. <https://doi.org/10.3390/cryst13060857>

Academic Editor: Jagdish K. Vij

Received: 2 May 2023

Revised: 16 May 2023

Accepted: 18 May 2023

Published: 23 May 2023



Copyright: © 2023 by the author. Licensee MDPI, Basel, Switzerland. This article is an open access article distributed under the terms and conditions of the Creative Commons Attribution (CC BY) license (<https://creativecommons.org/licenses/by/4.0/>).

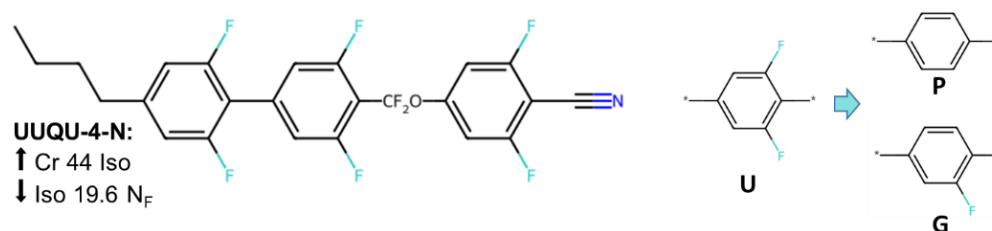


Figure 1. Molecular structure of UUQU-4-N, with transition temperatures (°C) taken from ref [25]. The up and down arrows indicate reported phase transitions on heating and cooling, respectively. Depiction of replacement of difluorobenzene (“U”) with either benzene (“P”) or fluorobenzene (“G”).

2. Method

Simulation Setup and Analysis

Fully atomistic molecular dynamics (MD) simulations were performed in Gromacs 2019 [26–32]. The ferroelectric nematic material UUQU-4-N (Figure 1) and its variants (*vide supra*) were modelled using the General Amber Force Field (GAFF) [33]. Atomic charges were determined using the RESP method [34] for geometries optimised at the B3LYP/6–31G(d) level of DFT [35,36] using the Gaussian G09 revision d01 software package [37]. Topologies were generated using AmberTools 16 [38,39] and converted into Gromacs readable format with AcPype [40].

We initially constructed a low-density lattice of 1000 molecules of UUQU-4-N with random positional and orientational order (500 molecules for variants). Following energy minimization by the steepest decent method, we performed short (5 ns) equilibration simulations in the NVE and NVT ($T = 600$ K) ensembles. We then performed a short ‘compression’ simulation (25 ns) at 600 K with an isotropic barostat ($P = 100$ Bar) to compress the simulation to a liquid-like density (~ 1.1 g cm³). The resulting isotropic configuration was then used as a starting configuration for *apolar* nematic simulations (UUQU-4-N only).

We obtained a *polar* nematic configuration by applying a static electric field (1 V nm^{−1}) along the x -axis of the isotropic starting configuration for a total of 100 ns at 288 K and 1 Bar. The resulting configuration was then used as the starting configuration for all *polar nematic* simulations (UUQU-4-N and variants).

For production MD simulations of UUQU-4-N—both *apolar* or *polar*—we used an anisotropic barostat with a pressure of 1 Bar, at temperatures of 258–348 K in 10 K increments for a further 1 μ s, unless otherwise noted. For variants, we performed production MD simulations starting from the polar configuration only; we perform simulations for 250 ns at 10 K above and below the simulated T_{Nf-Iso} of UUQU-4-N.

Simulations employed periodic boundary conditions in xyz . Bonds’ lengths were constrained to their equilibrium values with the LINCS algorithm [41]. During production MD simulations, the system pressure was maintained at 1 Bar using an anisotropic Parrinello–Rahman barostat [42,43]. Compressibilities in xyz dimensions were set to 4.5×10^{-5} , with the off-diagonal compressibilities set to zero to ensure the simulation box remained rectangular. Simulation temperature was controlled with a Nosé–Hoover thermostat [44,45]. Long-range electrostatic interactions were calculated using the Particle Mesh Ewald method with a cut-off value of 1.2 nm. A van der Waals cut-off of 1.2 nm was used. MD trajectories were visualised using PyMOL 4.5. Q-tensor analysis was performed using MDTraj 1.9.8 [46]. Cylindrical distribution functions (CDF) were computed using the *cylindr* code. [47] Simulation densities, dipole moments, and volumes were obtained with the *gmx energy* program, with dipole and volume being used to compute spontaneous polarisation.

We judged a simulation to be ‘nematic’ when the second-rank orientational order parameter ($\langle P_2 \rangle$) takes a value of >0.3 , and, conversely, we judge it isotropic if $\langle P_2 \rangle$ is below this value. We calculate $\langle P_2 \rangle$ via the Q-tensor according to Equation (1):

$$Q_{\alpha\beta} = \frac{1}{N} \sum_{m=1}^N \frac{3a_{m\alpha}a_{m\beta} - \delta_{\alpha\beta}}{2} \quad (1)$$

where N is the number of monomers; m is the monomer number within a given simulation; α and β represent the Cartesian x , y , and z axes; delta is the Kronecker delta; and a is a vector that describes the molecular long axis, which is computed for each monomer as the eigenvector associated with the smallest eigenvalue of the inertia tensor. The director at each frame was defined as the eigenvector associated with the largest eigenvalue of the ordering tensor. The order parameter, $\langle P2 \rangle$, corresponds to the largest eigenvalue of $Q_{\alpha\beta}$, and the biaxial order parameter, $\langle B \rangle$, corresponds to the difference between the two smallest eigenvalues. The polar order parameter, $\langle P1 \rangle$, was calculated as the total dipole moment of the simulation box over the sum of the individual molecular dipoles. The polarization, P , was calculated from the total dipole of the box over the volume.

3. Results

We start by considering apolar simulations that begin from an isotropic starting configuration. We find that *UUQU-4-N* does not spontaneously form a classical apolar nematic phase during MD simulations at any of the temperature ranges studied (278–358 K, Table S1). We also performed simulations beginning from a pseudo-nematic starting configuration at a temperature of 288 K; however, the orientational order decays within a few hundred nanoseconds to give an isotropic liquid (Figure S1).

For the polar simulations, our initial starting configuration was obtained by application of a large (0.1 V nm^{-1}) static electric field parallel to the simulation x -axis at a temperature of 288 K; this yields a polar nematic phase with $\langle P2 \rangle$ of 0.73 ± 0.02 , $\langle P1 \rangle = 0.95 \pm 0.03$, and $\langle B \rangle = 0.01 \pm 0.01$. The large values of $\langle P1 \rangle$ and $\langle P2 \rangle$ here are sustained by the applied field; we remove the field and perform a short relaxation simulation at the same temperature for 10 ns, after which we obtain $\langle P2 \rangle$ of 0.71 ± 0.03 , $\langle P1 \rangle = 0.93 \pm 0.04$, and $\langle B \rangle = 0.01 \pm 0.02$. From this configuration, we studied the evolution of each order parameter at a range of temperatures (258–358 K, 10 K increments). Plots of simulation order parameters ($\langle P1 \rangle$, $\langle P2 \rangle$, and $\langle B \rangle$), density, and spontaneous polarisation as a function of temperature are given in Figure 2; tabulated data are given in the Supplementary Materials to this article (Table S1).

Examination of the behaviour of both the polar ($\langle P1 \rangle$) and orientational ($\langle P2 \rangle$) order parameters as a function of temperature shows that, above a temperature of 318 K, the simulations evolve into an isotropic liquid; below this, $\langle P2 \rangle$ is consistent with the nematic order. The value at 318 K is a borderline case, and is on the cusp of being nematic (or isotropic, depending on perspective), and we suggest that this is the clearing point of our simulation. It should be noted that the present simulations overestimate the clearing point; recall that the experimental value for *UUQU-4-N* is 293 K.

The polar order parameter ($\langle P1 \rangle$) remains large and near-saturated in simulations at and below the clearing point. We do not observe transformation from polar to apolar nematic at any point, which indicates that the head-to-tail flipping of molecules is largely arrested. In all cases, the biaxial order parameter ($\langle B \rangle$) is negligible. There is a subtle increase in density at the Iso– N_F transition which results from the enhanced packing in the polar nematic configuration. Lastly, the large values of $\langle P1 \rangle$ coupled with a high density and large molecular electric dipole moment conspire to generate giant values of spontaneous polarisation which are comparable in magnitude to *RM734*, both experimental and *in silico*. We consider that these simulations are a reasonable approximation of the experimental reality of the N_F phase of *UUQU-4-N*.

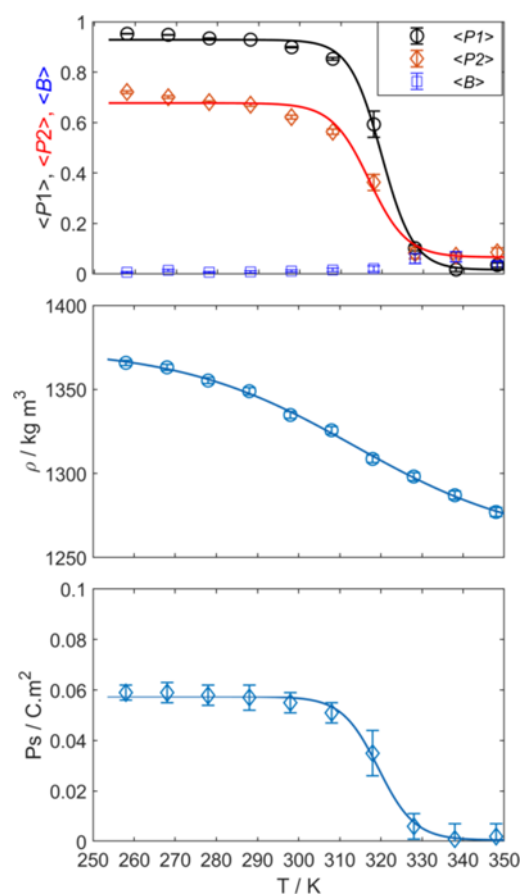


Figure 2. From top to bottom: simulation properties as a function of temperature: order parameters ($\langle P1 \rangle$, $\langle P2 \rangle$, and $\langle B \rangle$); density, kg m^3 ; and spontaneous polarisation, $\text{C}\cdot\text{m}^2$. Average values are given as data points, error bars show one standard deviation from the mean, and dashed lines are fits to the data which are presented as a guide to the eye. Fits take the form $A + (B - A)/(1 + \exp(-4 * \log(3) * (x - c)/D))$.

Cylindrical Pair Correlation Functions

The cylindrical pair correlation function (CDF) is related to the commonly encountered radial distribution function, differing in its use of cylindrical rather than spherical shells. The CDF gives information on anisotropic positional correlations between molecules, and can be used for ‘inverse design’ by revealing specific intermolecular interactions which may be of interest. Briefly, the CDF is computed by finding adjacent molecular centres of mass in cylindrical bins. This analysis is conducted over some range of cylinder length (denoted as h) and radius (denoted as r), for all time steps in the simulation. At each time step, the cylinder length is reoriented to be parallel to the nematic director.

We computed the CDF for polar nematic simulations in the temperature range 258 K to 338 K, i.e., from deep into the N_F phase ($T < 318$ K) to close to the N_F -Iso transition ($T = 318$ K) and finally into the isotropic liquid ($T > 318$ K).

We start by considering the N_F phase, the CDF of which presents as a concentric set of arc-like features which result from preferred pairing modes. As can be seen in Figure 3, there are two major overlapping arc-like features located on the axis (i.e., $r \sim 0$ Å) at $h = \pm 18$ – 22 Å, which result from head-to-tail pairing. The major off-axis feature is a pair of lobes at $r \sim 5$ Å and $h \sim \pm 5$ Å, indicating a preference for staggered parallel pairs of molecules; additional off-axis arcs centred on $r \sim 5$ Å (at $h \sim \pm 10$ Å and $h \sim \pm 13$ Å) result from analogous pairing modes with increased longitudinal intermolecular separation. As the temperature is increased, the features become less well-defined; for example, at a temperature of 288 K, we find two lobes at $r \sim 5.5$ Å and $h \sim \pm 5$ Å, which converge to a single feature by 318 K.

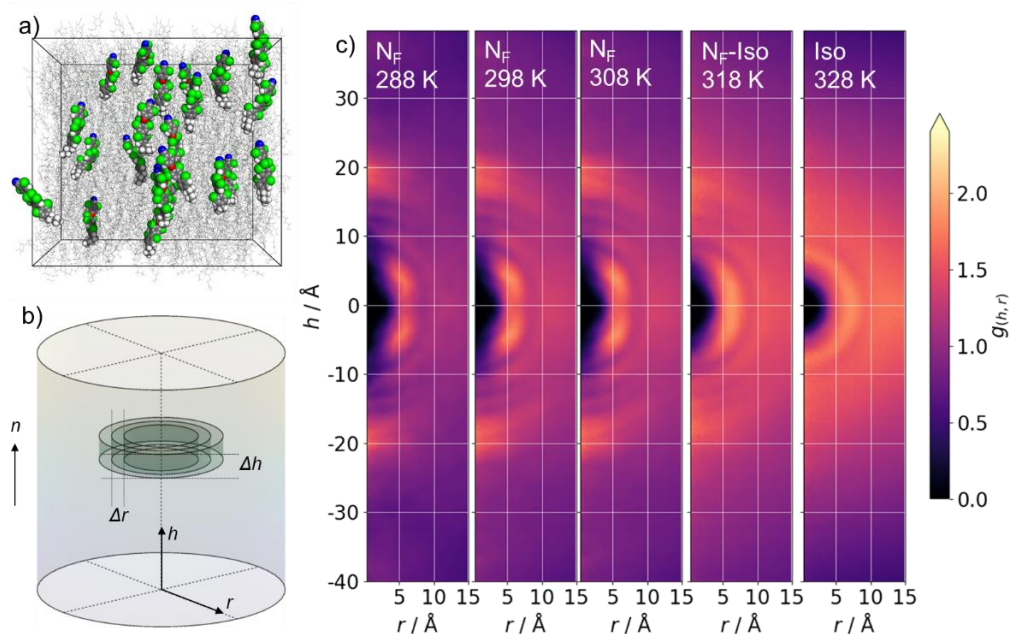


Figure 3. (a) Instantaneous configuration of an MD simulation of UUQU-4-N in the polar nematic configuration at a temperature of 298 K and at a time of 697 ns. To aid visualisation, only a small number of molecules are shown as space filling, with the rest rendered as wire. (b) Schematic of the cylindrical binning process used to generate the cylindrical distribution plots; the nematic director (n), cylinder length (h), and radius (r) are all indicated. (c) Evolution of the CDF computed for MD simulations of UUQU-4-N at the indicated temperatures.

Contrast this with the isotropic phase, where the only observed feature is a diffuse circle centred at $h = r = 0$ with radius ~ 8 Å, which results from the spatial proximity of the nearest neighbours. In both isotropic and polar nematic configurations, we find a region of zero probability centred at $h = r = 0$ Å, which results from steric repulsion.

Next, we extract the molecular indices and time steps for a given feature present in the CDF at some spatial region, enabling us to visualise representative instantaneous configurations for a given CDF region (Figure 4). Starting with the on-axis peaks located at $h = \pm 18$ – 22 Å, we find that the multiplicity of features that result from head-to-tail pairs has its origins in the conformation of the terminal chain. For $h = \pm 21$ – 22 Å, the butyl chain is predominantly in its all-*trans* form, whereas there is, predominantly, a single *gauche* conformer for the second major peak at $h = \pm 18$ – 19 Å.

In the case of $h = \pm 21$ – 22 Å, the head/tail of the mesogenic units of the interacting molecules are ~ 1.1 nm apart (distance between any non-alkyl atoms, averaged over all pairs in selection). At this separation, we can calculate that, with a dipole moment of circa 11 Debye (the average over the entire simulation) and an average angle between molecules of 30° (calculated from $\langle P_2 \rangle = 0.622$ at 298 K), the dipole–dipole interaction strength is small (~ 4.8 kJ mol $^{-1}$) and not much larger than $k_B T$. The presence of a single *gauche* conformer allows the mesogenic units of the pair to be closer; at $h = \pm 18$ – 19 Å, the separation between cores is just 0.7 nm on average which, using the same values as above, gives a dipole–dipole interaction strength of ~ 18.5 kJ mol $^{-1}$.

The presence of alkyl chains in UUQU-4-N causes longitudinal separation, weakening the dipole–dipole interactions. This is partly overcome by conformational effects, with a single *gauche* conformer enabling a proximal head-to-tail interaction which enables a polar order to take hold. For chains longer than butyl, the alkyl chain is akin to a spacer between molecules, separating to the point that the dipole–dipole interactions that generate a polar order cannot manifest. Experiments demonstrated that increased terminal chain length suppresses the incidence of the N_F phase some time ago, and our results here provide an explanation for this behaviour.

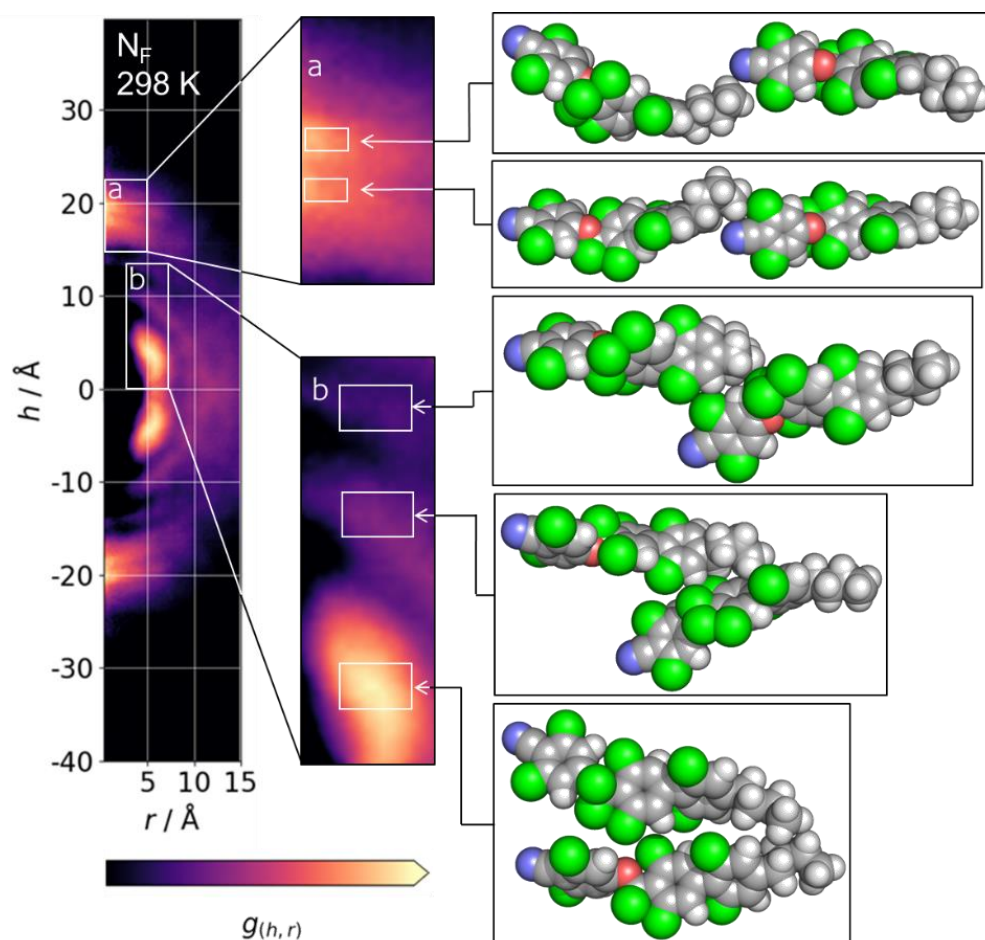


Figure 4. CDF for the N_F phase of UUQU-4-N at 298 K with logarithmic colour scale to aid visualisation of CDF features; expansions (a) and (b) show preferred pairing modes for head-to-tail and side-to-side pairs, respectively. White boxes in the expansions (a) and (b) show the spatial cut-offs used to look up pairs of molecules which were then selected randomly.

With regard to off-axis arcs, there are three prominent features centred at $r \sim 5$ Å and with h in the range $(\pm) 5$ – 15 Å; these result from staggered side-by-side pairs of molecules, with the major feature being the lobes at $\sim \pm 5$ Å. Weaker features are seen at $h \sim \pm 10$ and ± 14 . Each of these side-by-side configurations results from the electrostatic interaction of ArF atoms with ArH.

For RM734 (and related materials), intermolecular interactions between carboxylate esters appear to be a driver of polar order [2,3], with the loss of this group generally eliminating the N_F phase [11]. UUQU-4-N bears a difluoromethyleneoxy (CF_2O) linker; however, we do not see features in the CDF that result from analogous interactions between CF_2O groups. The replacement of the CF_2O group in UUQU-4-N with a carboxylate ester might therefore give a modest increase in the onset temperature of the N_F phase by introducing an additional intermolecular interaction capable of supporting a polar order, with this presumably being at the cost of an increased melting point.

Next, we simulated variants of UUQU-4-N in which we make changes to explore how these alter the relative stability of the polar nematic ordering. Specifically, we sought to investigate: the effects of altering the alkyl chain length; the effect of replacing the CF_2O group with CO_2 ; and the effect on altering the fluorination pattern on the mesogenic core (Figure 5).

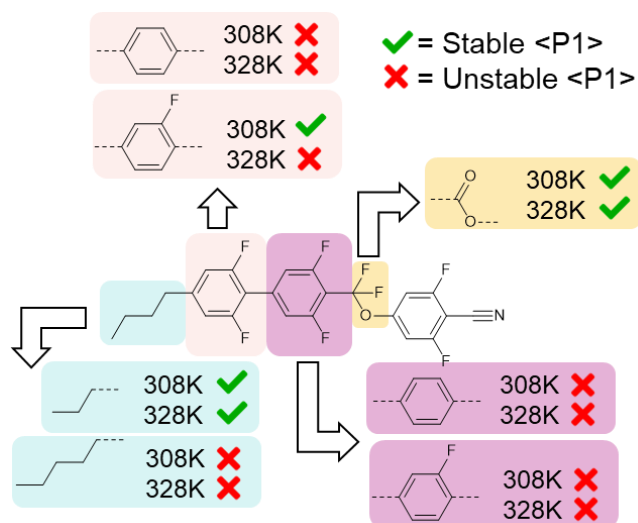


Figure 5. Effect of indicated structural variations on the stability of the N_F phase at a given temperature. A green tick indicates the polar nematic order is retained at this temperature, while a red cross indicates it is eliminated.

Firstly, we replaced one of the difluorobenzene rings of the biphenyl fragment of UUQU-4-N with either fluorobenzene or benzene, giving four variant materials (GUQU-4-N, PUQU-4-N, UGQU-4-N, and UPQU-4-N). We also generated a variant in which we replaced the difluoromethoxy linker with a carboxylate ester (a.k.a. UUZU-4-N), and two variants with either a propyl or pentyl chain *in lieu* of the butyl chain of the parent material (UUQU-3-N and UUQU-5-N, respectively). For each structure, we generated GAFF parameters with RESP charges as described for UUQU-4-N, with the initial MD configurations of 500 molecules then subjected to the same energy minimisation and equilibration protocols. We obtain polar nematic configurations by applying a static electric field. Finally, we perform a 250 ns production MD simulation at temperatures of 308 K and 328 K, i.e., 10 K above and below the simulated N_F -Iso point in the parent material. If the variant exhibits a stable polar nematic order at 328 K, it has an enhanced propensity to generate an N_F phase relative to the parent, with the inverse argument being true of variants whose polar nematic ordering decays to an isotropic liquid at 308 K. We judge a phase as stable when its polar order parameter ($\langle P1 \rangle$) does not vary by more than 10% from its initial value (which was >0.9 in all cases).

For virtually all variants, the polar nematic order was found to decay to an isotropic liquid within the first 50 ns of the simulation. The replacement of the CF_2O group with an ester appears to increase the clearing point; i.e., the thermal stability of the N_F phase is enhanced. Similarly, shortening the terminal chain from butyl to propyl also increases the clearing point, with the 328 K simulation retaining its polar order; however, the corresponding increase to pentyl eliminates polar ordering. Altering the fluorination pattern on the core eliminated the N_F phase in all but one case; the loss of a fluorine atom from the first ring appears to be tolerated, albeit with a reduction in clearing point.

4. Conclusions

UUQU-4-N is a remarkable material with a monotropic room-temperature N_F phase. Atomistic MD simulations can competently reproduce a stable polar nematic configuration, albeit with a slight overestimation in the isotropisation temperature. An analysis of the anisotropic cylindrical correlation function reveals how polar-pair formation persists in spite of the longer-than-optimal terminal chain length, and largely results from the interaction between regions of opposite electrostatic potential. It is found that, *in silico*, it is possible to boost the N_F transition temperature and give materials which might be somewhat more practical for experimental work. However, the simulations as performed

here give no indication of the likely melting point of these materials, which may render them less practical than the parent material. Ordinarily, the extension of the alkyl chain length would be a convenient way to engineer the melting and clearing points of a liquid crystal; however, we have shown that the propensity of alkyl chains of even modest length to disrupt the polar ordering of the N_F phase suggests this approach is futile in the present case.

Supplementary Materials: The following supporting information can be downloaded at: <https://www.mdpi.com/article/10.3390/cryst13060857/s1>, Figure S1: Plot of $\langle P_2 \rangle$ as a function of simulation time (ps) for an MD simulation of UUQU-4-N beginning from a pseudo-nematic starting configuration at a temperature of 288 K; Figure S2: Schematic overview of the CDF process; Figure S3: Evolution of the CDF over time; Table S1: Orientational order parameter ($\langle P_2 \rangle$) and simulation density (g cm^{-3}) as a function of temperature for simulations beginning from an isotropic initial configuration. Regardless of the temperature employed, nematic order fails to spontaneously emerge; Table S2: Tabulated data for key properties of atomistic simulations of UUQU-4-N beginning in a polar nematic configuration.

Funding: UK Research and Innovation (UKRI) via a Future Leaders Fellowship, grant no. MR/W006391/1.

Data Availability Statement: The data associated with this paper are openly available from the University of Leeds Data Repository at <https://doi.org/10.5518/1355> (accessed on 22 May 2023).

Acknowledgments: R.J.M. gratefully acknowledges funding from UK Research and Innovation (UKRI) via a Future Leaders Fellowship, grant no. MR/W006391/1, and from the University of Leeds via a University Academic Fellowship. Computational work was undertaken on ARC4, part of the high-performance computing facilities at the University of Leeds, UK.

Conflicts of Interest: The authors declare no conflict of interest.

References

1. Mertelj, A.; Cmok, L.; Sebastian, N.; Mandle, R.J.; Parker, R.R.; Whitwood, A.C.; Goodby, J.W.; Copic, M. Splay nematic phase. *Phys. Rev. X* **2018**, *8*, 041025. [[CrossRef](#)]
2. Chen, X.; Korblova, E.; Dong, D.; Wei, X.; Shao, R.; Radzihovsky, L.; Glaser, M.A.; Maclennan, J.E.; Bedrov, D.; Walba, D.M.; et al. First-principles experimental demonstration of ferroelectricity in a thermotropic nematic liquid crystal: Polar domains and striking electro-optics. *Proc. Natl. Acad. Sci. USA* **2020**, *117*, 14021–14031. [[CrossRef](#)] [[PubMed](#)]
3. Mandle, R.J.; Sebastián, N.; Martínez-Perdiguero, J.; Mertelj, A. On the molecular origins of the ferroelectric splay nematic phase. *Nat. Commun.* **2021**, *12*, 4962. [[CrossRef](#)]
4. Kikuchi, H.; Matsukizono, H.; Iwamatsu, K.; Endo, S.; Anan, S.; Okumura, Y. Fluid layered ferroelectrics with global ∞ symmetry. *Adv. Sci.* **2022**, *9*, 2202048. [[CrossRef](#)]
5. Chen, X.; Martínez, V.; Nacke, P.; Korblova, E.; Manabe, A.; Klasen-Memmer, M.; Freychet, G.; Zhernenkov, M.; Glaser, M.A.; Radzihovsky, L. Observation of a uniaxial ferroelectric smectic a phase. *arXiv* **2022**, arXiv:2206.12965. [[CrossRef](#)] [[PubMed](#)]
6. Sebastian, N.; Cmok, L.; Mandle, R.J.; de la Fuente, M.R.; Drevensek Olenik, I.; Copic, M.; Mertelj, A. Ferroelectric-ferroelastic phase transition in a nematic liquid crystal. *Phys. Rev. Lett.* **2020**, *124*, 037801. [[CrossRef](#)] [[PubMed](#)]
7. Folcia, C.L.; Ortega, J.; Vidal, R.; Sierra, T.; Etxebarria, J. The ferroelectric nematic phase: An optimum liquid crystal candidate for nonlinear optics. *Liq. Cryst.* **2022**, *49*, 899–906. [[CrossRef](#)]
8. Sebastian, N.; Mandle, R.J.; Petelin, A.; Eremin, A.; Mertelj, A. Electrooptics of mm-scale polar domains in ferroelectric nematic phase. *Liq. Cryst.* **2021**, *48*, 2055–2071. [[CrossRef](#)]
9. Máthé, M.T.; Buka, Á.; Jáklí, A.; Salamon, P. Ferroelectric nematic liquid crystal thermo-motor. *arXiv* **2022**, arXiv:2201.07556.
10. Mandle, R.J.; Cowling, S.J.; Goodby, J.W. A nematic to nematic transformation exhibited by a rod-like liquid crystal. *Phys. Chem. Chem. Phys.* **2017**, *19*, 11429–11435. [[CrossRef](#)]
11. Mandle, R.J.; Cowling, S.J.; Goodby, J.W. Rational design of rod-like liquid crystals exhibiting two nematic phases. *Chem. Eur. J.* **2017**, *23*, 14554–14562. [[CrossRef](#)] [[PubMed](#)]
12. Mandle, R.J.; Cowling, S.J.; Goodby, J.W. Structural variants of rm734 in the design of splay nematic materials. *Liq. Cryst.* **2021**, *48*, 1780–1790. [[CrossRef](#)]
13. Li, J.; Nishikawa, H.; Kougo, J.; Zhou, J.; Dai, S.; Tang, W.; Zhao, X.; Hisai, Y.; Huang, M.; Aya, S. Development of ferroelectric nematic fluids with giant- ϵ dielectricity and nonlinear optical properties. *Sci. Adv.* **2021**, *7*, eabf5047. [[CrossRef](#)]
14. Zhao, X.; Zhou, J.; Li, J.; Kougo, J.; Wan, Z.; Huang, M.; Aya, S. Spontaneous helielectric nematic liquid crystals: Electric analog to helimagnets. *Proc. Natl. Acad. Sci. USA* **2021**, *118*, e2111101118. [[CrossRef](#)] [[PubMed](#)]
15. Pocięcha, D.; Walker, R.; Cruickshank, E.; Szydłowska, J.; Rybak, P.; Makal, A.; Matraszek, J.; Wolska, J.M.; Storey, J.M.D.; Imrie, C.T.; et al. Intrinsically chiral ferronematic liquid crystals. *arXiv* **2021**, arXiv:2112.11887.

16. Saha, R.; Nepal, P.; Feng, C.; Sakhawat Hossein, M.; Gleeson, J.T.; Sprunt, S.; Twieg, R.J.; Jakli, A. Multiple ferroelectric nematic phases of a highly polar liquid crystal compound. *arXiv* **2021**, arXiv:2104.06520. [[CrossRef](#)]
17. Brown, S.; Cruickshank, E.; Storey, J.M.D.; Imrie, C.T.; Pocięcha, D.; Majewska, M.; Makal, A.; Gorecka, E. Multiple polar and non-polar nematic phases. *ChemPhysChem* **2021**, *22*, 2506–2510. [[CrossRef](#)]
18. Li, J.; Wang, Z.; Deng, M.; Zhu, Y.; Zhang, X.; Xia, R.; Song, Y.; Hisai, Y.; Aya, S.; Huang, M. General phase-structure relationship in polar rod-shaped liquid crystals: Importance of shape anisotropy and dipolar strength. *Giant* **2022**, *11*, 100109. [[CrossRef](#)]
19. Song, Y.; Li, J.; Xia, R.; Xu, H.; Zhang, X.; Lei, H.; Peng, W.; Dai, S.; Aya, S.; Huang, M. Development of emergent ferroelectric nematic liquid crystals with highly fluorinated and rigid mesogens. *Phys. Chem. Chem. Phys.* **2022**, *24*, 11536–11543. [[CrossRef](#)]
20. Dai, S.; Li, J.; Kougo, J.; Lei, H.; Aya, S.; Huang, M. Polar liquid crystalline polymers bearing mesogenic side chains with large dipole moment. *Macromolecules* **2021**, *54*, 6045–6051. [[CrossRef](#)]
21. Cruickshank, E.; Walker, R.; Storey, J.M.D.; Imrie, C.T. The effect of a lateral alkyloxy chain on the ferroelectric nematic phase. *RSC Adv.* **2022**, *12*, 29482–29490. [[CrossRef](#)]
22. Cigl, M.; Podoliak, N.; Landovský, T.; Repčák, D.; Kužel, P.; Novotná, V. Dimethylamino terminated ferroelectric nematogens revealing high permittivity. *arXiv* **2023**, arXiv:2301.04865.
23. Mandle, R.J. Supramolecular ferroelectric nematic materials. *Liq. Cryst.* **2022**, *49*, 2019–2026. [[CrossRef](#)]
24. Nishikawa, H.; Shiroshita, K.; Higuchi, H.; Okumura, Y.; Haseba, Y.; Yamamoto, S.I.; Sago, K.; Kikuchi, H. A fluid liquid-crystal material with highly polar order. *Adv. Mater.* **2017**, *29*, 1702354. [[CrossRef](#)]
25. Manabe, A.; Bremer, M.; Kraska, M. Ferroelectric nematic phase at and below room temperature. *Liq. Cryst.* **2021**, *48*, 1079–1086. [[CrossRef](#)]
26. Berendsen, H.J.C.; van der Spoel, D.; van Drunen, R. Gromacs: A message-passing parallel molecular dynamics implementation. *Comput. Phys. Commun.* **1995**, *91*, 43–56. [[CrossRef](#)]
27. Lindahl, E.; Hess, B.; van der Spoel, D. Gromacs 3.0: A package for molecular simulation and trajectory analysis. *Mol. Model. Annu.* **2001**, *7*, 306–317. [[CrossRef](#)]
28. Van Der Spoel, D.; Lindahl, E.; Hess, B.; Groenhof, G.; Mark, A.E.; Berendsen, H.J. Gromacs: Fast, flexible, and free. *J. Comput. Chem.* **2005**, *26*, 1701–1718. [[CrossRef](#)]
29. Hess, B.; Kutzner, C.; van der Spoel, D.; Lindahl, E. Gromacs 4: Algorithms for highly efficient, load-balanced, and scalable molecular simulation. *J. Chem. Theory Comput.* **2008**, *4*, 435–447. [[CrossRef](#)]
30. Pronk, S.; Páll, S.; Schulz, R.; Larsson, P.; Bjelkmar, P.; Apostolov, R.; Shirts, M.R.; Smith, J.C.; Kasson, P.M.; van der Spoel, D.; et al. Gromacs 4.5: A high-throughput and highly parallel open source molecular simulation toolkit. *Bioinformatics* **2013**, *29*, 845–854. [[CrossRef](#)] [[PubMed](#)]
31. Abraham, M.J.; Murtola, T.; Schulz, R.; Páll, S.; Smith, J.C.; Hess, B.; Lindahl, E. Gromacs: High performance molecular simulations through multi-level parallelism from laptops to supercomputers. *SoftwareX* **2015**, *1–2*, 19–25. [[CrossRef](#)]
32. Páll, S.; Abraham, M.J.; Kutzner, C.; Hess, B.; Lindahl, E. Tackling exascale software challenges in molecular dynamics simulations with gromacs. In *Solving Software Challenges for Exascale*; Markidis, S., Laure, E., Eds.; Springer International Publishing: Cham, Switzerland, 2015; pp. 3–27.
33. Wang, J.; Wolf, R.M.; Caldwell, J.W.; Kollman, P.A.; Case, D.A. Development and testing of a general amber force field. *J. Comput. Chem.* **2004**, *25*, 1157–1174. [[CrossRef](#)] [[PubMed](#)]
34. Bayly, C.I.; Cieplak, P.; Cornell, W.; Kollman, P.A. A well-behaved electrostatic potential based method using charge restraints for deriving atomic charges: The resp model. *J. Phys. Chem.* **1993**, *97*, 10269–10280. [[CrossRef](#)]
35. Lee, C.; Yang, W.; Parr, R.G. Development of the colle-salvetti correlation-energy formula into a functional of the electron density. *Phys. Rev. B* **1988**, *37*, 785–789. [[CrossRef](#)]
36. Becke, A.D. Density-functional thermochemistry. III. The role of exact exchange. *J. Chem. Phys.* **1993**, *98*, 5648–5652. [[CrossRef](#)]
37. Frisch, M.J.; Trucks, G.W.; Schlegel, H.B.; Scuseria, G.E.; Robb, M.A.; Cheeseman, J.R.; Scalmani, G.; Barone, V.; Mennucci, B.; Petersson, G.A.; et al. *Gaussian G09 Revision d01*; Gaussian, Inc.: Wallingford, CT, USA, 2016.
38. Case, D.A.; Cheatham, T.E., III; Darden, T.; Gohlke, H.; Luo, R.; Merz, K.M., Jr.; Onufriev, A.; Simmerling, C.; Wang, B.; Woods, R.J. The amber biomolecular simulation programs. *J. Comput. Chem.* **2005**, *26*, 1668–1688. [[CrossRef](#)]
39. Wang, J.; Wang, W.; Kollman, P.A.; Case, D.A. Automatic atom type and bond type perception in molecular mechanical calculations. *J. Mol. Graph. Model.* **2006**, *25*, 247–260. [[CrossRef](#)]
40. Sousa da Silva, A.W.; Vranken, W.F. Acypype—Antechamber python parser interface. *BMC Res. Notes* **2012**, *5*, 367. [[CrossRef](#)]
41. Hess, B.; Bekker, H.; Berendsen, H.J.C.; Fraaije, J.G.E.M. Lincs: A linear constraint solver for molecular simulations. *J. Comput. Chem.* **1997**, *18*, 1463–1472. [[CrossRef](#)]
42. Parrinello, M.; Rahman, A. Polymorphic transitions in single crystals: A new molecular dynamics method. *J. Appl. Phys.* **1981**, *52*, 7182–7190. [[CrossRef](#)]
43. Nosé, S.; Klein, M.L. Constant pressure molecular dynamics for molecular systems. *Mol. Phys.* **1983**, *50*, 1055–1076. [[CrossRef](#)]
44. Nosé, S. A molecular dynamics method for simulations in the canonical ensemble. *Mol. Phys.* **1984**, *52*, 255–268. [[CrossRef](#)]
45. Hoover, W.G. Canonical dynamics: Equilibrium phase-space distributions. *Phys. Rev. A* **1985**, *31*, 1695–1697. [[CrossRef](#)] [[PubMed](#)]

46. McGibbon, R.T.; Beauchamp, K.A.; Harrigan, M.P.; Klein, C.; Swails, J.M.; Hernández, C.X.; Schwantes, C.R.; Wang, L.P.; Lane, T.J.; Pande, V.S. Mdtraj: A modern open library for the analysis of molecular dynamics trajectories. *Biophys. J.* **2015**, *109*, 1528–1532. [[CrossRef](#)]
47. Mandel, R.J. Implementation of a cylindrical distribution function for the analysis of anisotropic molecular dynamics simulations. *PLoS ONE* **2022**, *17*, e0279679. [[CrossRef](#)]

Disclaimer/Publisher’s Note: The statements, opinions and data contained in all publications are solely those of the individual author(s) and contributor(s) and not of MDPI and/or the editor(s). MDPI and/or the editor(s) disclaim responsibility for any injury to people or property resulting from any ideas, methods, instructions or products referred to in the content.